RSC Advances

PAPER

View Article Online
View Journal | View Issue

Cite this: *RSC Adv.*, 2022, **12**, 16805

Investigation of the structural, electrical, and dielectric properties of $La_{0.5}Sm_{0.2}Sr_{0.3}Mn_{1-x}Cr_xO_3$ for electrical application

Khouloud Abdouli,*[a] F. Hassini,[bc] W. Cherif,[a] P. R. Prezas,[d] M. P. F. Graça,[d] M. A. Valent,[d] O. Messaoudi,[e] S. Elgharbi,[f] Ahmed Dhahri[g] and L. Manai[e]

Received 21st February 2022
Accepted 15th May 2022

DOI: 10.1039/d2ra01006b

rsc.li/rsc-advances

In the present research, polycrystalline samples of $La_{0.5}Sm_{0.2}Sr_{0.3}Mn_{1-x}Cr_xO_3$ are prepared using the self-combustion method. Then, we have studied their crystalline structure, and dielectric and electrical properties. The X-ray diffraction study shows that all the samples exhibit a single phase with orthorhombic structure (space group *Pnma*). The studied samples were also characterized by complex impedance spectroscopy in a wide range of temperatures and frequency. AC conductivity analyses are used to study the transport property of the investigated samples. These analyses indicate that the conduction mechanism is strongly dependent on temperature and frequency. It is also found that the conductivity decreases with Cr concentration. Complex impedance analysis confirms the contributions of grain and grain boundaries in the conduction mechanism. Finally, the impedance spectra, characterized by the appearance of semicircle arcs at different temperatures, were well modeled in terms of equivalent electrical circuits to explain the impedance results.

1. Introduction

Perovskite manganites have been the subject of intense research efforts[1–5] due to the potential technological application of the so-called colossal magnetoresistance (CMR) behavior.[6–8] In the last two decades, experiments have focused on the effects of the application of an electric field on doped manganites. These systems are known to exhibit interesting electronic properties which are explained by many mechanisms.[9–12] The manganite oxides described by the general formula $Ln_{1-x}A_xMnO_3$, where Ln is a rare earth and A is an alkaline earth, have become every exciting materials for researchers not only for their interesting physical properties but also for their inherent ability to accommodate a wide range of elemental compositions and to display a wealth of structure variants. Lanthanum manganite ($LaMnO_3$) is one of the most broadly studied systems.[13,14] The ferromagnetic/electric properties of these materials can be achieved by varying the sintering conditions and by doping with various cations on both La and Mn sites.[15,16] In this paper, we have synthesized a set of samples of $La_{0.5}Sm_{0.2}Sr_{0.3}Mn_{(1-x)}Cr_xO_3$ with different Cr contents and we study its effect of Cr doping on the structural, electrical and dielectric properties of these compounds. Impedance spectroscopy was successfully employed to obtain clear information about the conduction and dielectric properties of these materials.

The elaboration technique used for this investigation is the glycine nitrate process, an aqueous autocombustion process initially developed by Chick in 1990 for the production of chromite and manganite powders (GNP).[17] Two reagents are required to begin redox reactions in autocombustion processes: the oxidizer and the fuel. Although metal nitrates are obvious oxidizers due to their excellent water solubility, ability to sustain combustion (high oxidizing power), and low cost, the nature of the fuel necessitates that it meet two criteria: it must be a good chelating agent to avoid selective precipitation during cation solution, as well as an effective reductant. Several possibilities are mentioned in the literature; the most common ones are urea, citric acid, and glycine. The amino acid glycine is recognized to be the most basic of all the

---

[a] Sfax University, Faculty of Sciences, B. P. 1171, 3000, Tunisia

[b] Research Unit of Valorization and Optimization of Exploitation of Resources, Faculty of Science and Technology of Sidi Bouzid, Kairouan University, 9100 Sidi Bouzid, Tunisia

[c] Laboratory of Physical Chemistry of Materials, Physics Department, Faculty of Sciences of Monastir, Monastir University, 5019 Monastir, Tunisia

[d] I3N – University of Aveiro, Aveiro, Portugal

[e] Physics Department, College of Sciences, University of Ha'il, Saudi Arabia

[f] Department of Chemistry, College of Science, University of Hail, Ha'il, Kingdom of Saudi Arabia

[g] Department of Physics, College of Science and Humanities - Dawadmi, Shaqra University, Riyadh, Saudi Arabia

amino acids. It has a zwitterionic nature due to its carboxylic acid and amine functionalities, allowing it to complex a high number of metal cations with its formula NH_2CH_2COOH. Indeed, the COO– group primarily captures alkalis and alkaline earths, whereas the amine typically complexes transition metals.[17,18] Concerning the reduction properties, the heats of combustion of the reducing agents given by Hwang are −2.98 kcal g^{-1}, −2.76 kcal g^{-1} and −3.24 kcal g^{-1} for urea, citric acid, and glycine respectively.[19] Glycine, in addition to being a strong chelating agent, appears to be the reductant most likely to make the autocombustion process the most exothermic.

2. Experimental procedure

2.1 GNP principles

The redox reaction equation for synthesis of $La_{0.5}Sm_{0.2}Sr_{0.3}Mn_{0.9}Cr_{0.1}O_3$ *via* the GNP method is as follows:

$$\begin{gathered}0.5La(NO_3)_3 + 0.2Sm(NO_3)_3 + 0.3Sr(NO_3)_2 + 0.9Mn(NO_3)_2\\ + 0.1Cr(NO_3)_3 + zNH_2CH_2COOH + \lambda O_2 \rightarrow\\ La_{0.5}Sm_{0.2}Sr_{0.3}Mn_{0.9}Cr_{0.1}O_3 + \delta CO_2 + \delta' H_2O + \delta'' N_2\end{gathered}$$

where z is the amount of glycine introduced in the reaction.

$$\frac{G}{N} = \frac{z}{(0.5 \times 3) + (0.2 \times 3) + (0.3 \times 2) + (0.9 \times 2) + (0.1 \times 3)} = \frac{Z}{4.8}$$

For a given fuel, the reaction is governed by the maximum temperature reached during combustion which is itself dependent on the oxidizing/reducing character of the mixture defined by the stoichiometric coefficient noted φ, which is the ratio between the total valences of the fuel (glycine) and the oxidizers (metal nitrates). These correspond to those defined in the Jain model:[20] +4 for carbon, +1 for hydrogen, +2 for strontium and manganese and +3 for lanthanum, samarium and the chromium, while nitrogen has a zero valence (0) and oxygen a negative valence of −2. φ is therefore calculated as

$$\varphi = \frac{Z\left[\left(2 \times 4_{(C)}\right) + \left(5 \times 1_{(H)}\right) + 0_{(N)} + \left(-2 \times 2_{(O)}\right)\right]}{\left|0.5\left[3_{(La)} + 3\left(0_{(N)} - 3 \times 2_{(O)}\right)\right] + 0.2\left[3_{(Sm)} + 3\left(0_{(N)} - 3 \times 2_{(O)}\right)\right] + 0.3\left[2_{(Sr)} + 2\left(0_{(N)} - 3 \times 2_{(O)}\right)\right] + 0.9\left[2_{(Mn)} + 2\left(0_{(N)} - 3 \times 2_{(O)}\right)\right] + 0.1\left[3_{(Cr)} + 2\left(0_{(N)} - 3 \times 2_{(O)}\right)\right]\right|}$$

follows:

Hence $\varphi = \dfrac{9Z}{24}$ and the G/N ratio becomes

$$\frac{G}{N} = \frac{24\varphi}{9 \times 4.8} = 0.55\varphi$$

By definition, the reaction is considered under stoichiometric conditions when $\varphi = 1$, *i.e.* when all the valences of the oxidizing and reducing elements compensate each other. G/N is then 0.55 and Z is equal to 2.64. It is in this case that the reaction is the most violent and that the temperature reached during combustion is maximum.

2.2 Experimental protocol

We mix stoichiometric ratio of nitrates, $La(NO_3)_3 \cdot 6H_2O$, $Sm(NO_3)_3 \cdot 6H_2O$, $Sr(NO_3)_2$, $Mn(NO_3)_2 \cdot 4H_2O$, $Cr(NO_3)_3 \cdot 9H_2O$ and glycine ($C_2H_5NO_2$) with high purity (Sigma Aldrich, >97%). All nitrates were dissolved in distilled water to form the precursor solution for $La_{0.5}Pr_{0.2}Sr_{0.3}Mn_{(1-x)}Fe_xO_3$ ($x = 0$, 0.15 and 0.2) composition. The precursor solution was heating on a hot plate at about 100 °C for 1 h under magnetic stirring. Water was gradually vaporized during heating and formed a transparent viscous gel. When a critical temperature was reached (350 °C), the autoignition started, lasting only few seconds combustion and a great deal of foams produced. The obtained powders were preheated at 350 °C for about 4 h to remove the remaining organic and decompose the nitrates of the gel. These powders were sintered at 600 and 800 °C for 12 h with pressing into pellets form (of about 1 mm in thickness) under 4 tonnes per cm^2.

Phase purity and homogeneity, of the synthesized materials were checked by X-ray diffraction (XRD) analysis (CuKα radiation $\lambda = 1.5405$ Å) at room temperature. The impedance spectroscopy measurements were taken in the temperature range 100–400 K with 10 K step and in the frequency range of 100 Hz to 1 MHz using an impedance analyzer HP 4294 A Precision Impedance meter in the Cp–Rp configuration. The samples were maintained in a helium atmosphere in order to improve the heat transfer and eliminate the moisture.

3. Results and discussions

3.1 Structural analysis

The Rietveld refinement of X-ray diffraction patterns for the prepared samples are shown in Fig. 1a and b. These diagrams show quite fine and intense lines, which shows the good crystallization of the synthesized samples. They also show the absence of additional peaks related to other impurity phases, thus confirming the purity of the prepared samples. These spectra are characterized by strong main lines which can be identified (using the X'Pert HighScore Plus program) as corresponding to an orthorhombic phase with the *Pnma* space group. The quality of the refinement is evaluated through the goodness of the fit indicator χ^2. The refined crystallographic data and relevant geometrical parameters for all the samples are listed in Table 1. An enlargement at the scale of the most intense line (121) represented in the inset of Fig. 1 reveals that according to the rate of substitution x of the chromium, the angular position of Bragg shifts towards the large angles, sign a decrease in the lattice parameters of the synthesized samples. A reduction of the unit cell volume and the lattice parameters is expected upon substitution manganese by chromium because the radius of Cr^{3+} (0.615 Å) is a little smaller than that of Mn^{3+} (0.645 Å).[21] The bond lengths d_{Mn-O} and the bond angle Mn–O–Mn change slightly with increasing Cr^{3+} content.

The crystallite size was calculated using the full width at half maximum (FWHM) of the most intense peak (1 1 0) by Scherrer's formula:[22]

$$D = \frac{K\lambda}{\beta\cos(\theta)} \tag{1}$$

where $\lambda = 1.5406$ Å is the wavelength for CuKα radiation, θ is the diffraction angle of the most intense peak, K is the shape factor equal to 0.9, β is the full width at half maximum of the highest peak. The average crystallite sizes are listed in Table 1.

The distortion from the ideal perovskite structure was confirmed with the value of the Goldschmidt[23] tolerance factor.

$$t = \frac{(r_A + r_O)}{\sqrt{2}(r_B + r_O)} \tag{2}$$

where r_A, r_B and r_O are respectively the average ionic radii of the A and B perovskite sites and of the oxygen anion. In the ideal case ($t = 1$), the structure is cubic, for $0.96 < t < 1$, rhomboidal distortions occur and for $t < 0.96$, the distortions are orthorhombic.

3.2 Electrical conductivity

The conductivity data are analyzed using Jonscher's law.[24]

$$\sigma_T(\omega) = \sigma_{dc} + \sigma_{ac}(\omega) = \sigma_{dc} + A(T)\omega^{n(T)} \tag{3}$$

where $\sigma_T(\omega)$ is the total conductivity; σ_{dc} is the frequency independent term giving the conductivity in continuous current, $\sigma_{ac}(\omega)$ is the pure dispersive component of the conductivity in alternative current having a characteristic of power law in terms of angular frequency ω, A is the temperature dependent constant and "n" is an exponent, which represents the degree of interaction between ions and their surroundings, represents an imperative source of information about the model for the conduction mechanism in the material.

In order to evaluate the conductivity of our samples and to identify the origin of the conduction process, it is useful to present the ac conductivity at different frequencies and temperatures which can be calculated from the dielectric data using following formula:

$$\sigma_{ac} = \omega\varepsilon_0\varepsilon_r \tan\delta \tag{4}$$

where ε_r is relative dielectric constant.[25]

The frequency dependent conductivity spectrum is plotted in Fig. 2a which shows two distinct regions, a low frequency plateau region and a high frequency dispersive region. As

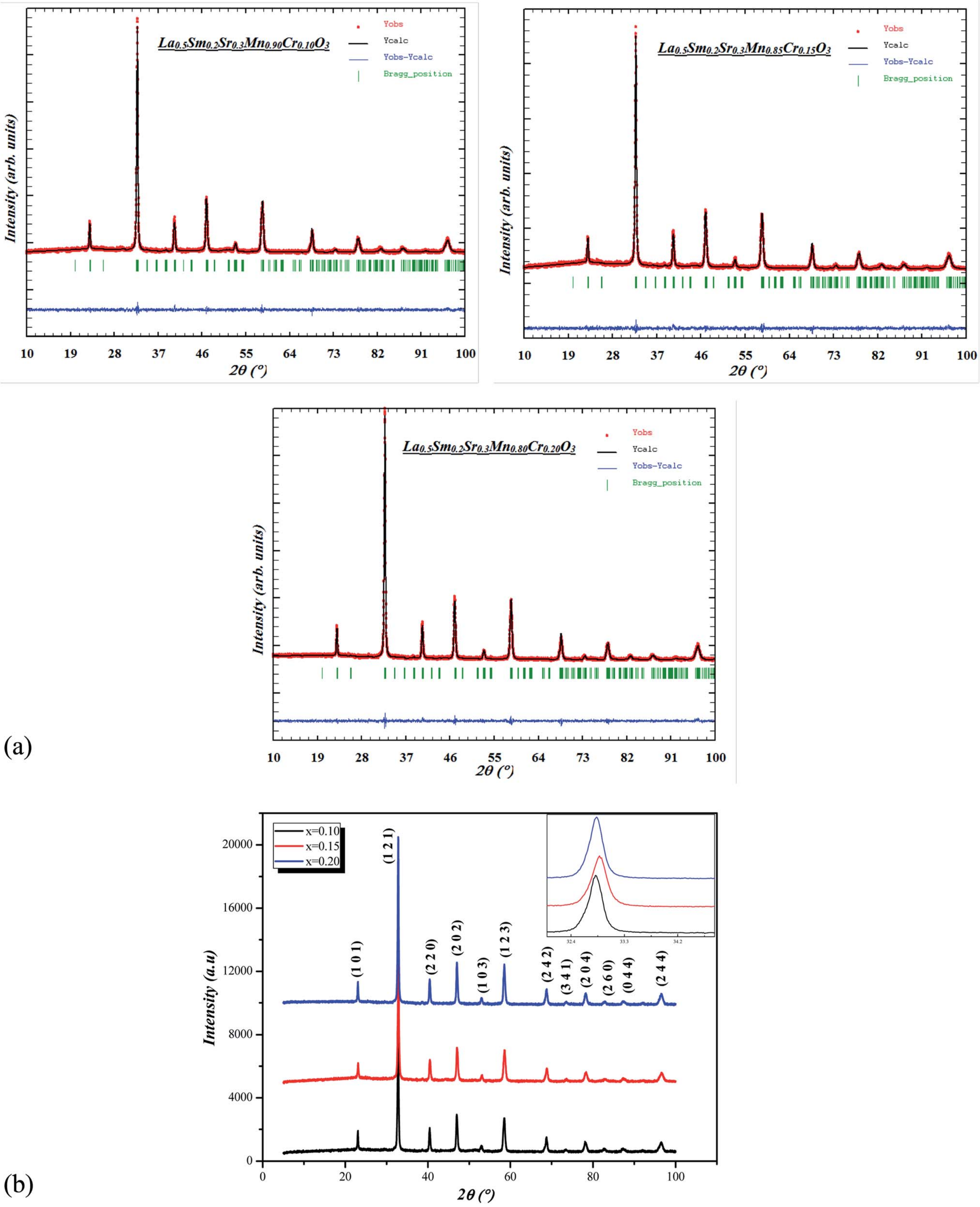

Fig. 1 a) Observed and calculated X-ray diffraction data and Rietveld refinement for $La_{0.5}Sm_{0.2}Sr_{0.3}Mn_{1-x}Cr_xO_3$ ($x = 0.10$, 0.15 and 0.20). Vertical bars are the Bragg reflections for the space group *Pnma*. The difference pattern between the observed data and fits is shown at the bottom. (b) X-ray diffraction pattern of $La_{0.5}Sm_{0.2}Sr_{0.3}Mn_{1-x}Cr_xO_3$ ($x = 0.00$, 0.10, 0.15 and 0.20).The peaks are indexed in the *Pnma* space group. The inset shows observed XRD profiles of the most intense peaks (Bragg reflections 121).

Table 1 Results of Rietveld refinements, determined from XRD patterns measured at room temperature for $La_{0.5}Sm_{0.2}Sr_{0.3}Mn_{1-x}Cr_xO_3$ ($x = 0.10$, 0.15, and 0.20) compounds

Parameters	$x = 0.10$	$x = 0.15$	$x = 0.20$
Symmetry	Orthorhombic	Orthorhombic	Orthorhombic
Space group	*Pnma*	*Pnma*	*Pnma*
a (Å)	5.496(5)	5.491(4)	5.489(9)
b (Å)	7.718(6)	7.713(7)	7.717(9)
c (Å)	5.462(6)	5.459(9)	5.460(8)
V (Å^3)	231.752(4)	231.27(6)	231.376(8)
d_{Mn-O1} (Å)	1.950(4)	1.949(4)	1.955(4)
d_{Mn-O2} (Å)	1.99(3)	1.86(6)	1.87(3)
d_{Mn-O2} (Å)	1.92(3)	2.02(6)	2.03(3)
d_{Mn-O} (Å)	1.955(4)	1.947(1)	1.953(8)
$\theta_{Mn-O1-Mn}$ (°)	163.36(17)	163.37(16)	161.44(15)
$\theta_{Mn-O2-Mn}$ (°)	165.2(14)	170.(3)	166.4(12)
$\theta_{Mn-O-Mn}$ (°)	164.28(7)	166.835(8)	163.926(7)
R_p (%)	3.19	3.39	3.74
R_{wp} (%)	4.04	4.25	4.79
R_{exp} (%)	3.61	3.73	4.16
Bragg *R*-factor (%)	1.78	1.59	1.57
RF-factor (%)	4.34	3.33	3.19
χ^2 (%)	1.25	1.30	1.33
D (nm)	32.38	31.50	27.15
t	0.85	0.85	0.85

frequency increases, hopping between charge carriers increases which results an increase in AC conductivity value of all samples. At any frequency, conductivity is found to decrease with the increase in chrome concentration. To understand the transport behaviors of our material system, one must suppose that the doping element's electronic structure is critical. In our situation, the doped element is chromium, which is a periodic table neighbor of manganese, and these ions occur in the forms Mn^{3+}, Mn^{4+}, and Cr^{3+} in such systems.[26] Cr^{3+}: ($t_{2g}^3e_g^0$) ($S = 3/2$), Mn^{3+}: ($t_{2g}^3e_g^1$) ($S = 2$), and Mn^{4+}: ($t_{2g}^3e_g^0$) ($S = 3/2$) are their electronic configurations, with only the (e_g^1) electron of Mn^{3+} being electrically active. Cr^{3+}, Mn^{3+}, and Mn^{4+} have ionic radii of 0.615 Å, 0.645 Å, and 0.530 Å, respectively.[27] Because the chromium ion's radius is approximately identical to that of the Mn^{3+} ion, the latter is immediately replaced by the Cr^{3+} form. Cr^{3+} has the same electronic configuration as Mn^{4+}, hence the FM double exchange FMDE interaction between Mn^{3+} and Cr^{3+} should be the same as between Mn^{3+} and Mn^{4+}.Then, in the semiconducting phase, inserting Cr^{3+} into manganite (Mn^{3+}–O–Mn^{4+} chains) disrupts the lattice by enhancing electron–phonon interaction, encouraging the creation of polarons and hopping between various valence states of Mn. Furthermore, it is well known that the FMDE interaction between Mn^{3+} and Cr^{3+} ions is weaker than the interaction between Mn^{3+} and Mn^{4+} ions.[28] As a result of Cr doping, the effective FMDE interaction weakens. Also, because of the weaker DE interaction, the single electrically active electron, e_g^1 electron of the Mn^{3+} ion, becomes confined, resulting in a steady drop in conductivity as Cr concentration rises. Moreover, this decrease in conductivity values can be related to the decrease in grain size. This can be explained by the fact that with a decrease in grain size the effect of grain boundaries opposes the passage of charge carriers which increases the barrier effect and thus the path to the decrease of electrical transport.

Fig. 2b illustrate a typical example of a non-linear fitting of frequency dependency of AC electrical conductivity for $La_{0.5}Sm_{0.2}Sr_{0.3}Mn_{0.85}Cr_{0.15}O_3$ sample at $T = 180$ K using the Jonscher's law. It can be seen that the fit (red solid line) matches well with the experimental values which means that the electrical conductivity are well fitted. The inset shows the variation of the exponent n as a function of temperature for the three samples ($x = 0.10$, 0.15 and 0.20). The conductivity parameters σ_{ac} for 100 Hz, n, and A values are summarized in Table 2. The n values decrease with increasing the concentration of chrome indicating that the electron-hopping decrease with addition of this metal which confirm the precedent results.

According to Funke,[29] the electrons-hopping is happened between neighboring sites for both samples $x = 0.10$ and $x = 0.15$ as their n values are greater than unity, which is the case of other materials.[30–32] Whereas for the sample $x = 0.20$ n is found to be between 0.8 and 1 for temperatures lower than $T = 200$ K. This can be ascribed to hopping conduction of mobile charge carriers (ions) over barrier between two sufficiently distant sites. This behavior is similar to that observed in amorphous semiconductors and glasses.[33–36]

Furthermore, based on the variation of the exponent n as a function of temperature we identify the predominant conduction process for our present compounds. Different models have been proposed to determine the conduction's nature, such as the Quantum Mechanical Tunneling (QMT),[37] the Correlated Barrier Hopping (CBH) model,[38] the Non-overlapping Small Polaron Tunneling (NSPT) model,[39] and the Overlapping Large Polaron Tunneling (OLPT) model.[40] In our case we notice an increase in the n values with increasing temperature which is corresponding to a thermally activated process. From this behavior we can reveal that the NSPT model is most suitable model to describe the conduction mechanism in our compounds.

It was important to note that a significant number of materials have been recognized to exhibit small polaron conduction as a result.[41,42] The Coulomb interaction between conduction electrons and the lattice ionic charge carrier produces a quasiparticle that results in a strong electron phonon coupling. Virtual phonons surround conduction electrons, which equate to the electron drawing nearby positive ions towards it and pushing nearby negative ions away. The electrons and their virtual phonon, which may be thought of as a new quasi-composite particle, are known as polarons, and they polarize the system by modifying the energy state configurations. We also remark that for an electron placed in a continuum polarizable (or deformable) medium, the electron mobility and effective mass estimation, which results in an alleged small and large polaron, the radius of the polaron is significantly bigger than the lattice constant of the materials in large polaron, which is also known as Fröhlich polaron. The wave function of a large polaron and its accompanying lattice distortions was characterized by a dimensionless number known as the Fröhlich coupling constant (), which was distributed over

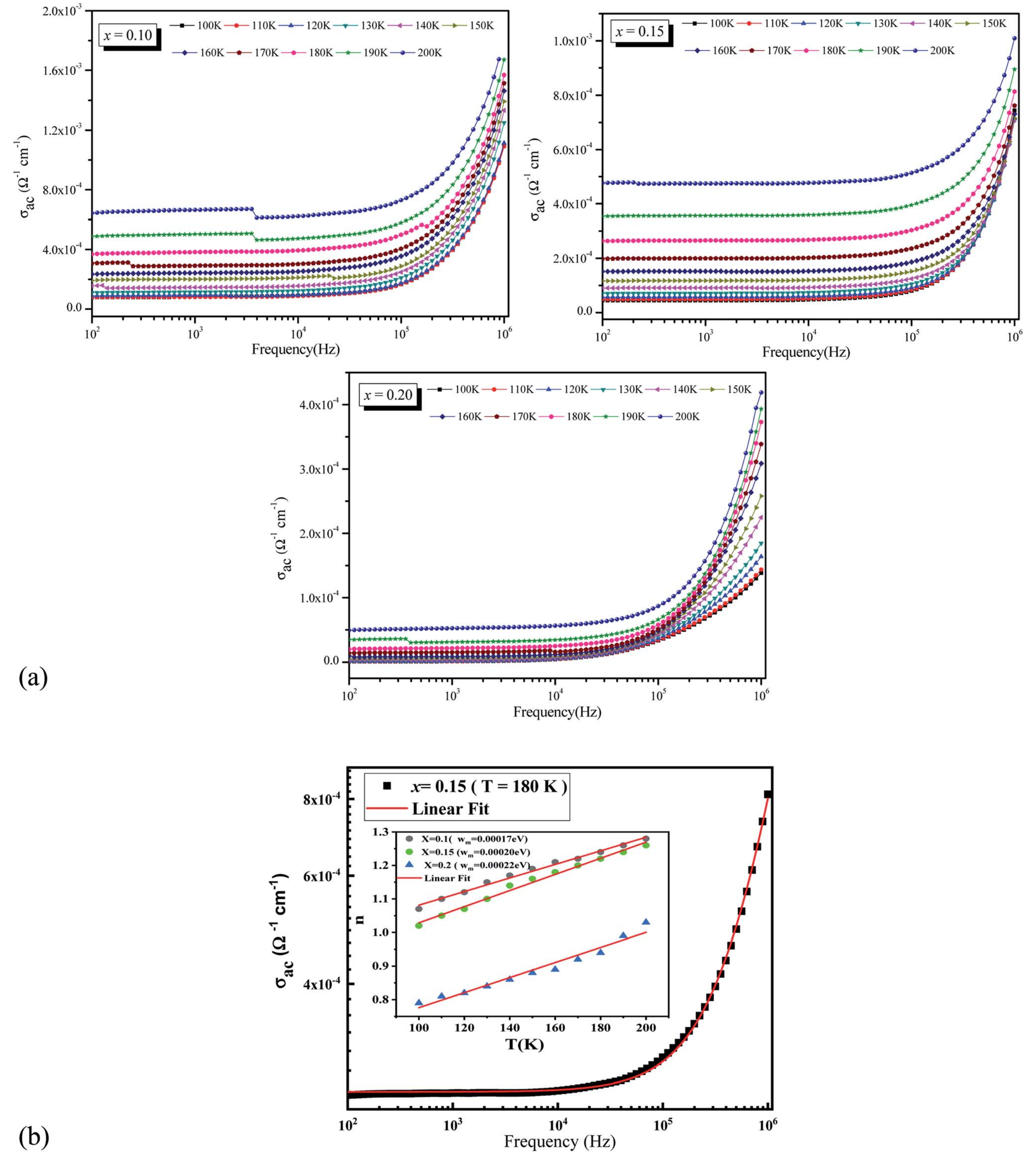

Fig. 2 (a) Frequency dependence of ac conductivity (σ_{ac}) at various temperatures of $La_{0.5}Sm_{0.2}Sr_{0.3}Mn_{1-x}Cr_xO_3$ (x = 0.10, 0.15 and 0.20). (b) Typical example (conductivity *vs.* frequency at T = 180 K for x = 0.15) fitted using the universal *Jonscher* power law. The inset shows the variation of the exponent n *vs.* temperature for (x = 0.10, 0.15 and 0.20).

several lattice sites. As a result of the expansion of effective mass, polarizations of ionic carriers can pursue polaron motion due to limited phonon frequencies and inseminate *via* lattice sites as free electrons with low kinetic energy. The small polaron of thermally activated hopping is created when the deformation surrounding charge carriers and their ionic displacement is constrained to a volume of one unit or less to its nearest neighbor.

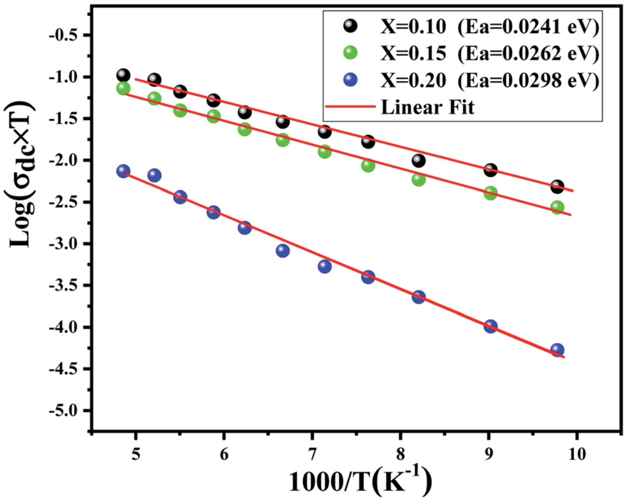

Fig. 3 Dependence of $\log(\sigma_{dc} \times T)$ on $(1000/T)$. Red solid lines represent the linear fit to the experimental data.

Table 3 Parameters used to NSPT model fitting for the $La_{0.5}Sm_{0.2}Sr_{0.3}Mn_{1-x}Cr_xO_3$ ($x = 0.10$, 0.15 and 0.20) compounds

Sample	$N(E_F)$ (10^{38} eV^{-1} m^{-1})	α (A$^{\circ -1}$)	W_H (eV)
$x = 0.10$	0.96	1.14	0.145
$x = 0.15$	17.8	1.35	0.245
$x = 0.20$	35.47	1.89	0.298

The exponent n can be expressed as a function of temperature by the following formula:[43]

$$n(T) = 1 + \frac{4k_BT}{W_m} \tag{5}$$

where k_B is the Boltzmann constant, and the W_m represents the bonding energy of charge carriers.

The W_m values were calculated from the slope of the $n(T)$ curves in the NSPT model. The values are obtained in the order of 0.00017 eV, 0.00020, and 0.00022 eV for $x = 0.10$ and 0.15, and 0.20 respectively. The insertion of chrome in place of manganese has an effect on the bonding energy. Indeed the increase of W_m values in agreement with the decrease of the conductivity when we rise Cr concentration.

The dc conductivity behavior is well fitted by the Arrhenius relation given as[44]

$$\sigma_{dc} = \sigma_0 \exp\left(-\frac{E_{dc}}{k_BT}\right). \tag{6}$$

where σ_0 is a pre-exponential factor and k_B is the Boltzmann constant. Eqn (2) is being used to calculate the activation energies (E_{dc}) required in the samples by plotting the graph of $\log(\sigma_{dc} \times T)$ *vs.* $(1000/T)$ in Fig. 3. From this figure, we can see that the dc conductivity decreases with Cr substitution. This decrease in σ_{ac} values can be related to the decrease of the grain size. The E_{dc} value expected from the linear fitting of the curves are of the order of 0.0241 eV for $x = 0.10$ and 0.0262 eV for $x = 0.15$ and 0.0298 eV for $x = 0.20$. In addition, according to the NSPT model, the conductivity can be described by the following expression[45]

$$\sigma(w) = \frac{(\pi e^2)k_BT\alpha^{-1}w\left[N(E_F)^2\right]R_w{}^2}{12} \tag{7}$$

Whither R_w is the tunneling distance is calculated by the following relation:

$$R_w = \frac{1}{2\alpha}\left[\ln\left(\frac{1}{w\tau_0}\right) - \frac{w_H}{k_BT}\right] \tag{8}$$

In eqn (7) and (8), the term α^{-1} is the spatial extension of the polaron, $N(E_F)$ represents the density of states near the Fermi level and W_H is the polaron hopping energy. The $N(E_F)$, α and W_H were adjusted to fit the calculated curves of $\log(\sigma_{dc} \times T)$ *vs.* $(1000/T)$ on the experimental curves. The obtained parameters are summarized in Table 3. As seen clearly that the $N(E_F)$ values are reasonably high which confirms that the hopping between

Table 2 Fitting parameters using Jonscher power law obtained from the experimental data of Ac conductivity as a function of frequency different temperatures for $La_{0.5}Sm_{0.2}Sr_{0.3}Mn_{1-x}Cr_xO_3$ ($x = 0.10$, 0.15, and 0.20) compounds

	$x = 0.1$			$x = 0.15$			$x = 0.20$		
T (K)	$\sigma_{ac} \times 10^{-5}$ (Ω^{-1} cm^{-1})	$A \times 10^{-10}$	n	$\sigma_{ac} \times 10^{-5}$ (Ω^{-1} cm^{-1}) (S m^{-1}) $\times 10^{-5}$	$A \times 10^{-10}$	n	$\sigma_{ac} \times 10^{-5}$ (Ω^{-1} cm^{-1})	$A \times 10^{-10}$	n
100	8.274	3.788	1.072	3.99	4.80	1.02	0.081	18.98	0.82
110	8.347	2.52	1.102	4.38	3.13	1.05	0.144	15.02	0.84
120	9.158	1.80	1.12	6.3	2.22	1.07	0.219	14.4	0.86
130	11.78	1.41	1.153	6.67	1.48	1.10	0.102	15.02	0.865
140	15.19	1.179	1.17	8.84	0.83	1.14	0.144	12.96	0.87
150	20	0.903	1.19	11.5	0.619	1.16	0.768	12.68	0.88
160	25.01	0.648	1.216	14.92	0.459	1.18	0.506	12.27	0.89
170	29.34	7.39	1.22	20	0.389	1.19	1.314	10.23	0.92
180	39.77	0.471	1.24	26.6	0.256	1.22	2.002	7.645	0.945
190	48.9	0.347	1.26	35.7	0.194	1.24	3.112	3.912	0.994
200	65	0.265	1.28	47.6	0.149	1.26	5.151	3.421	1.07

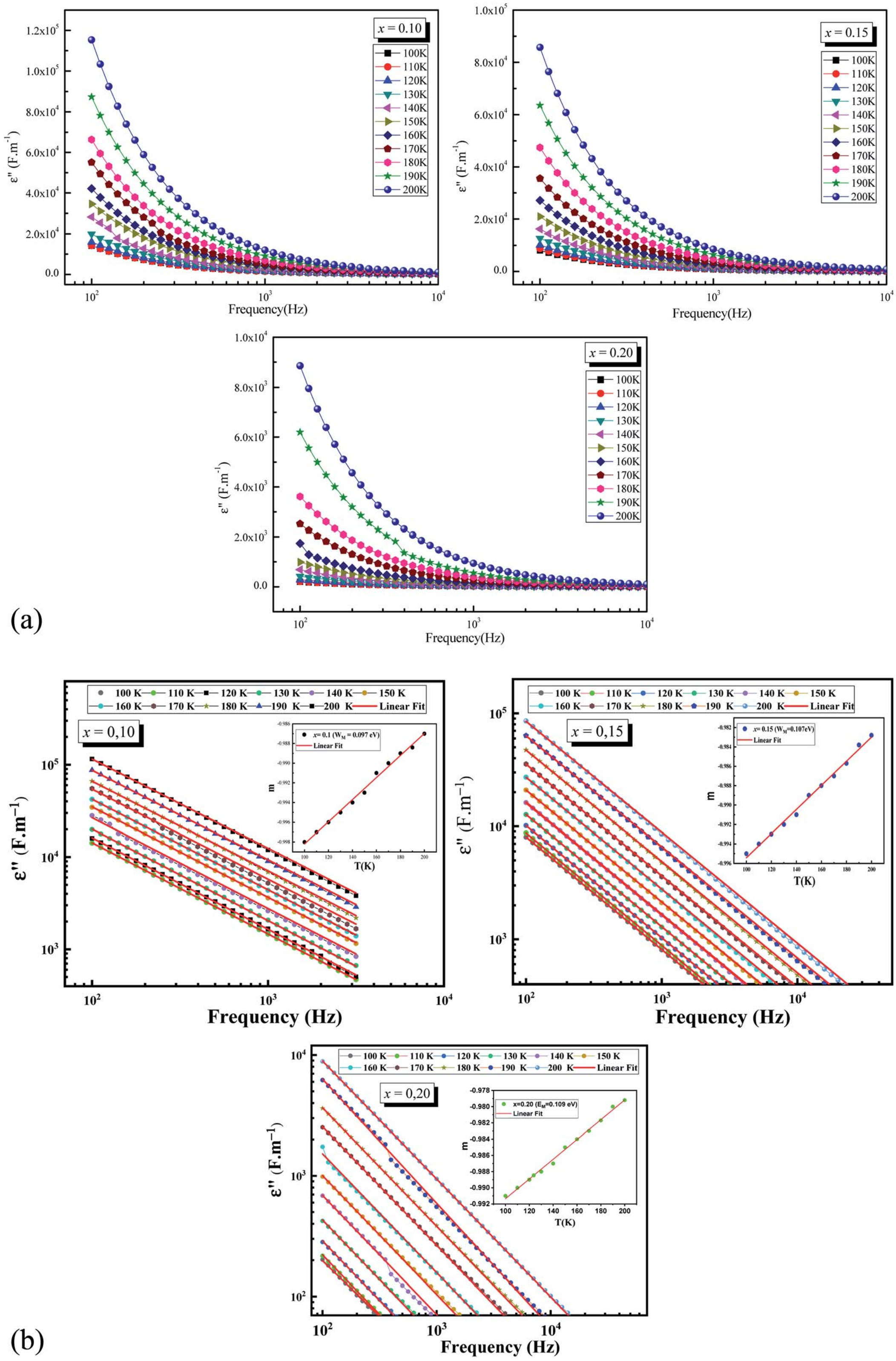

Fig. 4 a) Imaginary part of dielectric constant (ε'') *versus* Logarithm of (ω) at different temperatures for $La_{0.5}Sm_{0.2}Sr_{0.3}Mn_{1-x}Cr_xO_3$ ($x = 0.10$, 0.15 and 0.20). (b) Frequency dependence at different temperatures of the imaginary part of permittivity of $La_{0.5}Sm_{0.2}Sr_{0.3}Mn_{1-x}Cr_xO_3$ ($x = 0.10$, 0.15 and 0.20). Red solid lines represent the fit according to *Giuntini* equation. The insets show the temperature dependence of the parameter *m*.

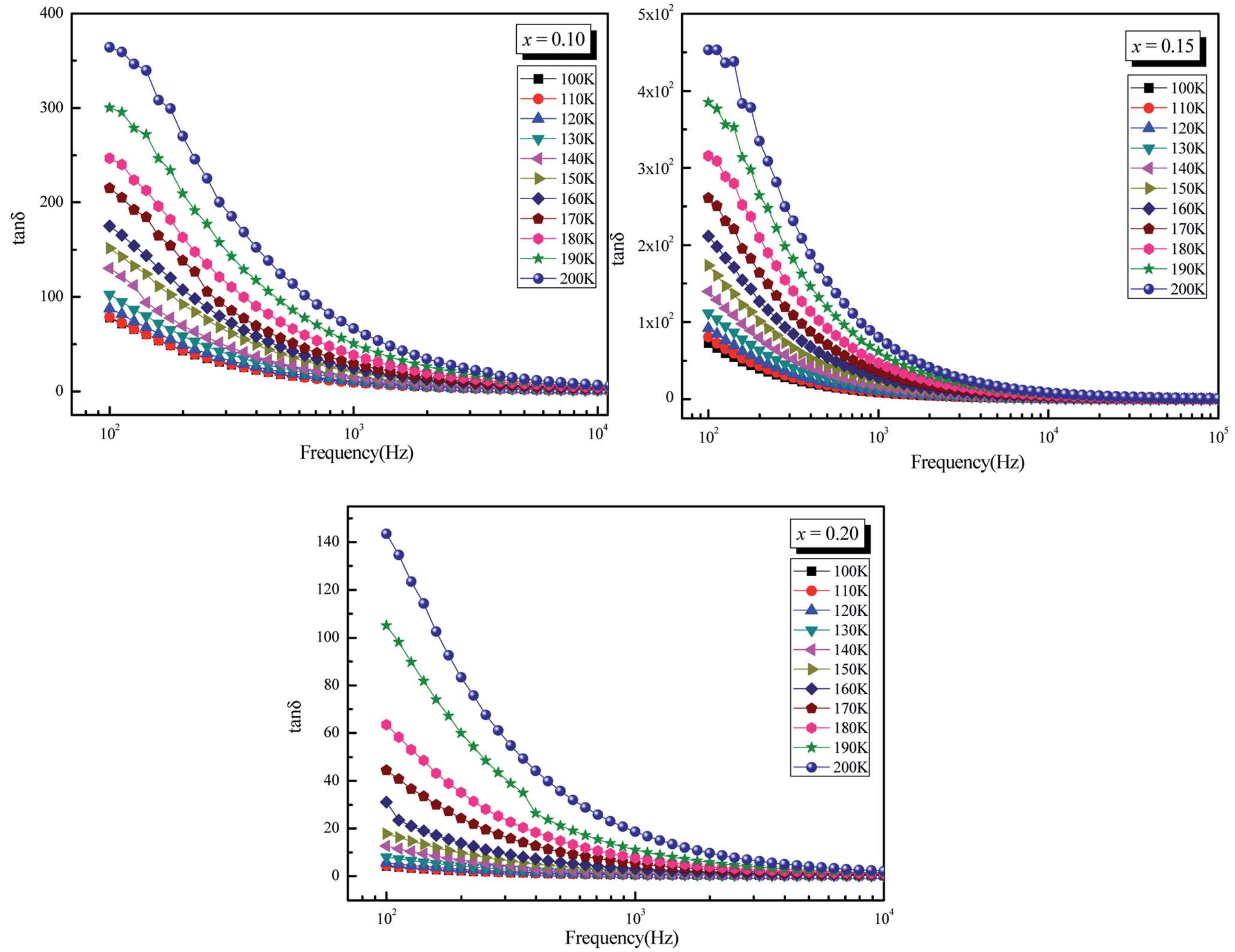

Fig. 5 Dielectric loss tangent (tan δ) *versus* Logarithm of (ω) at different temperatures for $La_{0.5}Sm_{0.2}Sr_{0.3}Mn_{1-x}Cr_xO_3$ (x = 0.10, 0.15 and 0.20).

site pairs dominates the charge transport mechanism in the prepared compounds.[46]

3.3 Dielectric studies

According to the Mott theory,[47] the complex permittivity is expressed as:

$$\varepsilon^* = \varepsilon' - j\varepsilon'' \tag{9}$$

where ε' (dielectric constant) and ε'' (dielectric loss) are the real and imaginary parts of the dielectric constant, respectively.

The dissipation factor or loss tangent (tan δ) can be expressed by the formula:

$$\tan\delta = \varepsilon''/\varepsilon' \tag{10}$$

The dielectric loss is the power dissipated in a dielectric as heat when the dielectric is exposed to an electric field. The origins of these dielectric losses, ε'', are the conduction losses, dipole losses and vibrational losses. Dielectric loss tangent (tan δ) is defined as a ratio of energy lost or dissipated per cycle to the energy stored.

The plots of imaginary part of permittivity ε'' and of loss tangent δ (tan δ) *versus* frequency at different temperatures for $La_{0.5}Sm_{0.2}Sr_{0.3}Mn_{(1-x)}Cr_xO_3$ (x = 0.10, 0.15 and 0.2) samples are showing in the Fig. 4.a and the Fig. 5 respectively. With increasing frequency, ε'' and tan δ values are found to decrease rapidly at low frequencies until they become frequency independent at higher frequencies which leads to the appearance of two different regions in $\varepsilon'' = f$(freq) and tan $\delta = f$(freq) spectra: a plateau region at higher frequency and a strong dielectric dispersion at lower frequency. This behavior can be explained by the Maxwell–Wagner interfacial polarization[48,49] where the dielectric permittivity of a material is due to the four types of polarizations:[50] interfacial, dipolar, ionic and electronic. The contribution of each type depends either on the frequency. Electronic and ionic polarizations are active in the high frequency range, while the other two mechanisms prevail in the low frequency range. Indeed the dielectric structure of manganite is composed of grains which act as good conductive, separated by grain boundaries which have the ability to act as an insulator, preventing the inter-grains conductivity. Under the influence of an electric field applied across the material, the

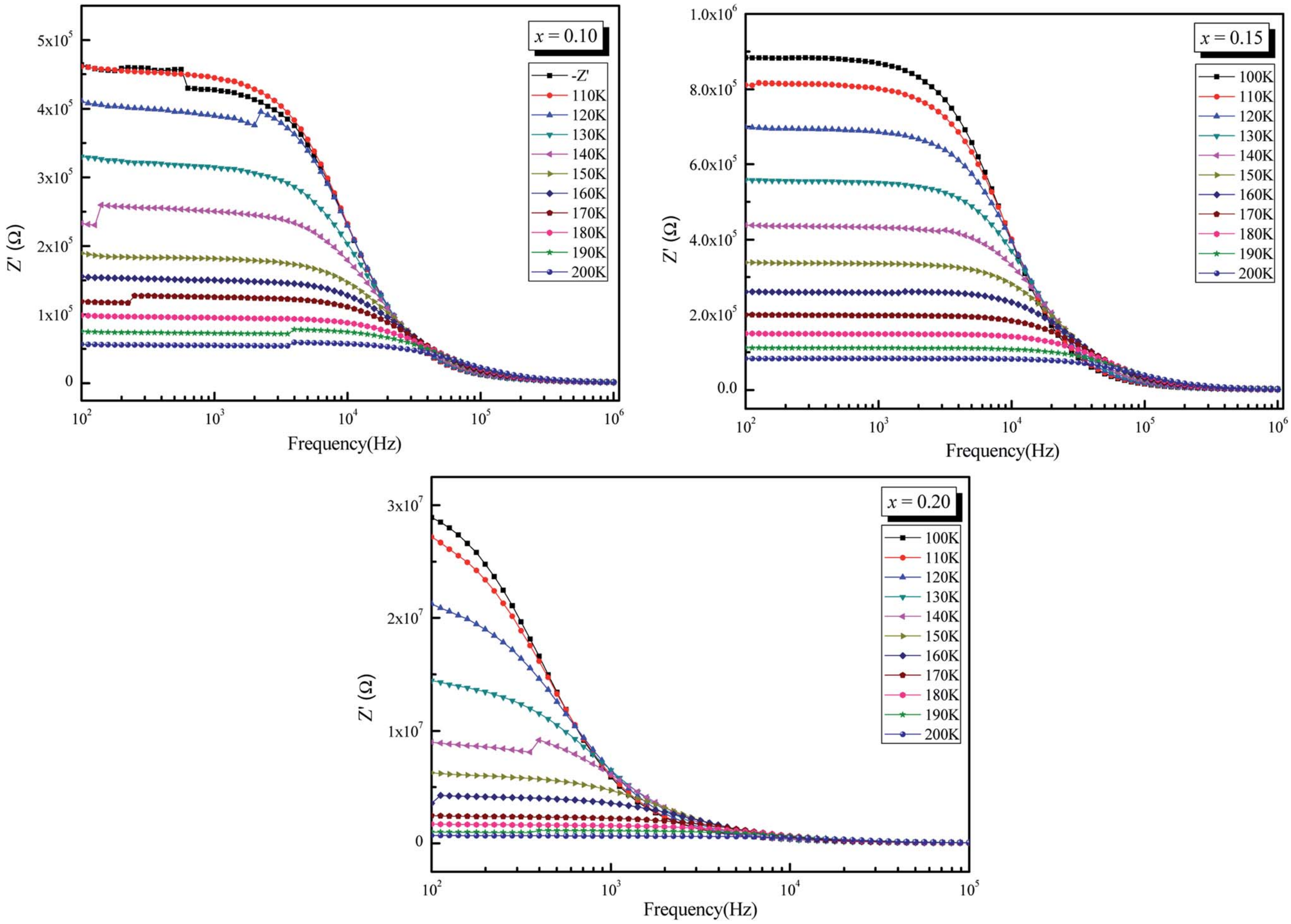

Fig. 6 Variation of real part of impedance (Z') as a function of frequency (ω) of $La_{0.5}Sm_{0.2}Sr_{0.3}Mn_{1-x}Cr_xO_3$ (x = 0.10, 0.15 and 0.20).

movement of electrons through the grain is interrupted in the grain boundaries. Charges accumulate in the interface between grains, therefore the appearance of interfacial polarization. We can attribute the dispersion occurring in the low frequency region to this interfacial polarization, since the effect of grain boundaries is dominant in the low frequency region. The electronic exchange results in a local displacement of the electrons in the electric field direction, which polarizes the samples. Thus, by increasing frequency, the polarization decreases. Beyond a certain frequency, the electrons in the grain can no longer follow the alternating field thus the electrons begin to localize, leading to the non-frequency dependence of dielectric constants. At the low-frequency region, the values of the loss factor decrease with increasing the chromium concentration in good agreement with the decrease of the conductivity. The low values of the two dielectric constants at higher frequencies identifies the potential of these material for high frequency applications.[51] Fig. 4a and 5 show an increase of ε'' and tan δ values with increasing temperature which can be attribute to the thermally activated nature of the hopping of charge carriers.

Moreover, we can use Giuntini model[52] to analyze ε'' (freq, T) spectra where ε'' can be expressed as:

$$\varepsilon''(\omega) = (\varepsilon_0 - \varepsilon_\infty)2\pi^2 N(ne/\varepsilon_0)^3 KT{\tau_0}^m {W_M}^{-4}\omega^m \tag{11}$$

With ε_0 is the static dielectric constants, ε_∞ is the optical dielectric constants, n is the number of the hopping charges, N is the concentration of localized sites, and W_M is the maximum barrier height.

The eqn (11) can be abbreviate as:

$$\varepsilon''(\omega) = B\omega^m \tag{12}$$

The variation of the exponent m *versus* temperature is presented in the insets of Fig. 4b. The m's values are estimated from the negative slopes of the obtained lines in Fig. 4b and it was found to increase linearly with temperature. It emerges, according to Giuntini model, that with varying temperature, $m(T)$ (dielectric properties) shows the same behavior of $n(T)$ (measurements of alternating current).

The exponent $m(T)$ may be written as a function of temperature and maximum barrier height W_M according to the following equation:

$$m = \frac{-4k_B T}{W_M} \tag{13}$$

W_M values witch are calculated from the last equation are found to be 0.097 eV, 0.107 eV and 0.109 eV for the samples x = 0.10, x =

0.15 and $x = 0.20$ respectively (insets of Fig. 4b). The WM values obtained are quite similar to those obtained using eqn (13).

3.4 Complex impedance analysis

Various contributions in electrical characteristics emanating from the system's grains and grain-boundaries may be distinguished using this impedance spectroscopy.[53,54] The real (Z') and imaginary (Z'') part of the complex impedance can be calculated by using the following equations:[55]

$$Z^* = Z' - jZ'' \tag{14}$$

where Z' and Z'' can be written as:

$$Z' = \frac{R_g}{1+\omega_g{}^2 C_g{}^2 R_g{}^2} + \frac{R_{gb}}{1+\omega_{gb}{}^2 C_{gb}{}^2 R_{gb}{}^2} \tag{15}$$

$$Z'' = \frac{R_g{}^2 \omega_g C_g}{1+\omega_g{}^2 C_g{}^2 R_g{}^2} + \frac{R_{gb}{}^2 \omega_{gb} C_{gb}}{1+\omega_{gb}{}^2 C_{gb}{}^2 R_{gb}{}^2} \tag{16}$$

where R_g, C_g are the resistance and capacitance resulting from the grain interiors while R_{gb}, C_{gb} represent these parameters from the grain boundaries.

The frequency dependence of real part of impedance (Z', *i.e.*, bulk resistance) at some representative temperature is shown in Fig. 6. It is clear from the $Z' = f(\text{freq})$ curves that the impedance value decreases with rise in frequency and temperature. The values of Z' merge after a certain frequency. This may be due to release of space charges at low temperatures.[56,57] The reduction in barrier properties of the materials with rise in temperature may be a responsible factor for enhancement of AC conductivity of the materials at higher frequencies.[58,59] Further, in the low frequency region, there is a decrease in magnitude of Z' with rise in temperature showing negative temperature coefficient of resistance (NTCR) behavior. This behavior is changed drastically in the high frequency region showing complete merger of plot above a certain fixed frequency. This particular frequency at which Z' value becomes constant is observed to shift towards the high-frequency side with rise of temperature. This shift in Z' plateau indicates the possibility of frequency relaxation process in the material.

Fig. 7 shows the frequency and temperature dependent plots of the imaginary part of impedance (Z'', *i.e.*, loss spectrum) for all the samples. This plot provides information on the dielectric processes taking place in the material. The Z'' value is shown to decrease with frequency for all temperatures and to shift to higher frequencies as the temperature increases. The spectrum is characterized by the appearance of a peak which is shifted to higher frequency with increasing temperature, indicating the

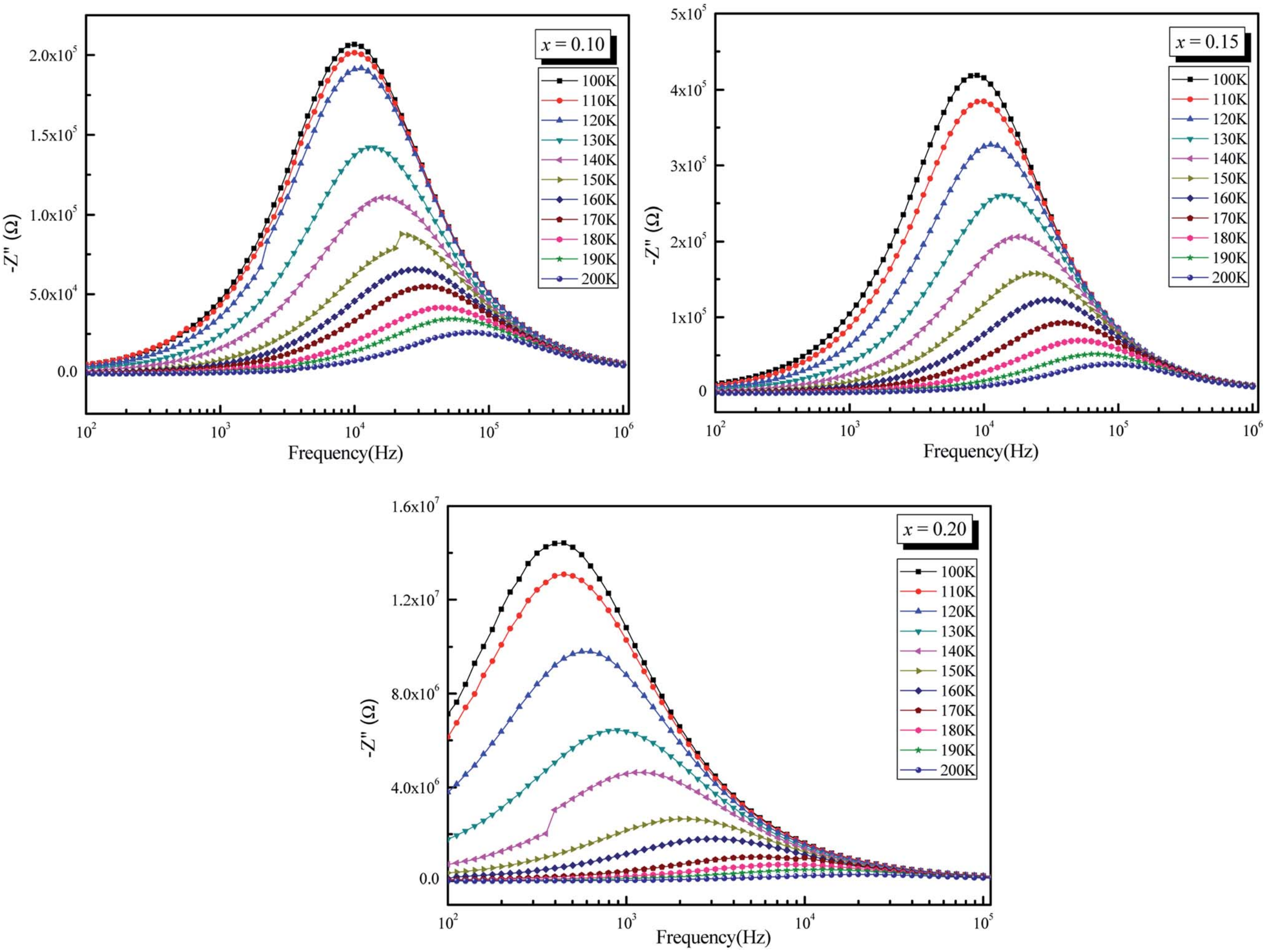

Fig. 7 Variation of imaginary part of impedance ($-Z''$) as a function of frequency (ω) of $La_{0.5}Sm_{0.2}Sr_{0.3}Mn_{1-x}Cr_xO_3$ ($x = 0.10$, 0.15 and 0.20).

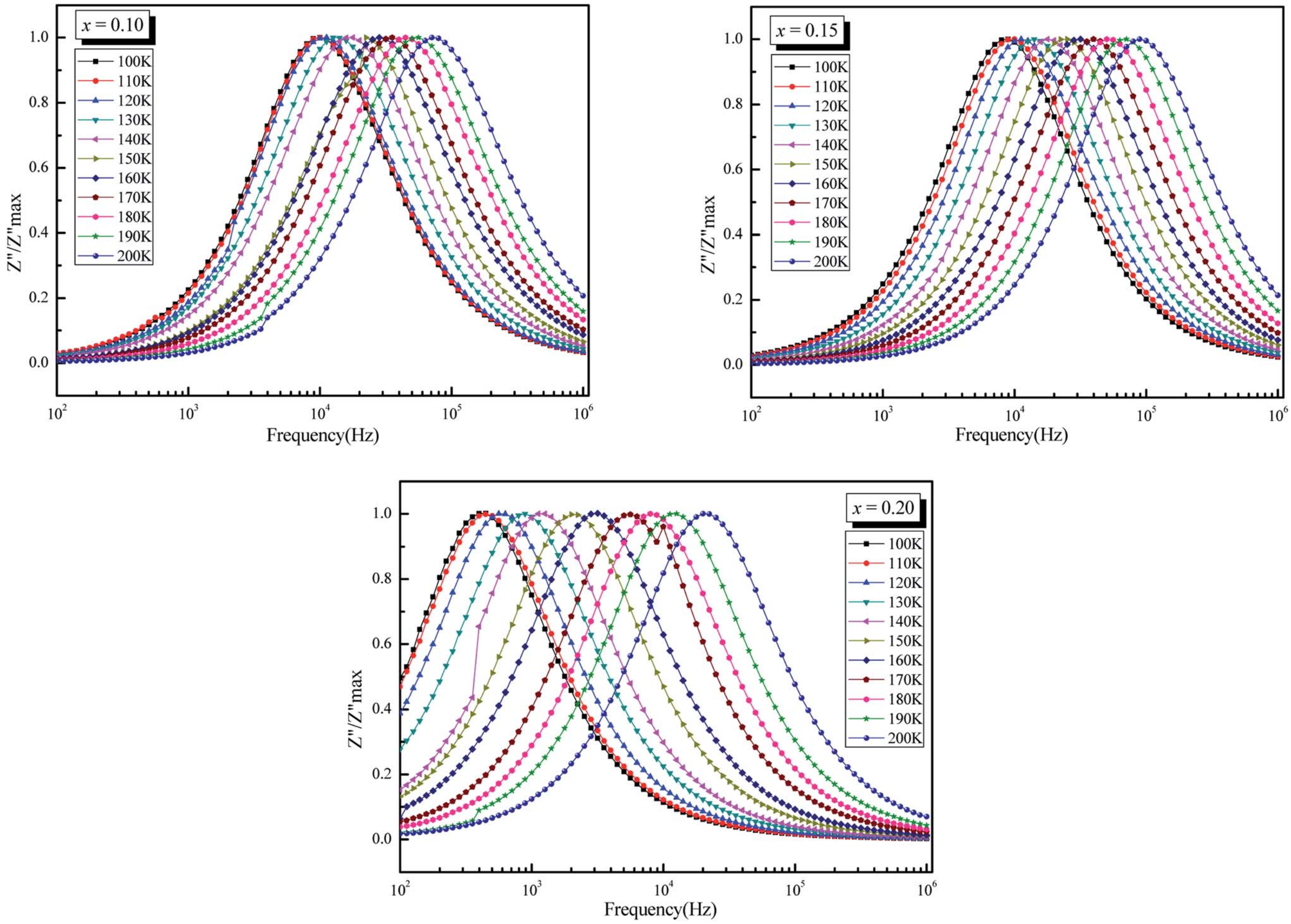

Fig. 8 Variation of Z''/Z'' max as a function of frequency (ω) of $La_{0.5}Sm_{0.2}Sr_{0.3}Mn_{1-x}Cr_xO_3$ ($x = 0.10$, 0.15 and 0.20).

existence of relaxation processes in the system, while its broadening on increasing temperature suggests that those relaxation processes are temperature-dependent.[60] At low temperatures, the relaxation phenomenon may be due to the immobile species/electrons; at high temperatures, the relaxation may be due to the defects/vacancies.[61]

The normalized spectra of Z'' (*i.e.* Z''/Z'' max) as function of frequency at different temperatures are represented in Fig. 8. These plots are normally used to detect the presence of the smallest capacitance and the largest resistance as suggested by Sinclair *et al.*[62] This will help us to identify the relaxation process whether there is a short range or long range motion of charge carriers. If the process is of short range, frequency dependence peaks of Z'' occurs at different frequencies but for long-range movement of charge carrier peaks occurs at the same frequency.[62,63] In the studied compounds, the mismatch of above two peaks of different temperatures suggests the presence of short-range motion of charge carrier.[62,64]

In order to determine the contributions of grain boundaries and grains (bulk or intrinsic properties of material) in the conduction mechanism, Cole–Cole analysis[65] has been performed. For all investigated samples, the Nyquist diagram ($-Z''$ *vs.* Z') at different temperatures is presented in Fig. 9a. As clearly shown, All the Nyquist plots are not centered on the real axis which indicating the departure from the ideal Debye behavior.[66,67]

We observe that the diameters of the semicircles decrease when temperature increases. Such behavior proves that the conduction process is thermally activated. The Nyquist plots are formed by two semicircles: a small one at high frequency due to bulk (grain) and a larger one at low frequencies due to grain boundary.[68] For ceramics materials, Nyquist plot is used in modeling the compound by an electrical equivalent circuit. Fig. 9b shows the simulate Nyquist plots with the equivalents circuits elements for $La_{0.5}Sm_{0.2}Sr_{0.3}Mn_{0.85}Cr_{0.15}O_3$ samples at several temperatures. The investigated compound can be modeled by an equivalent circuit model, which is composed of two parallel circuits. The first circuit describes the transport through the grain. It is composed of a resistor R_g and a constant phase element CPE1.The second one is composed of a resistor R_{gb} in parallel with a constant phase element CPE2.

The extracted parameters R_g, C_g, R_{gb}, Q, and α_{gb} are given in Table 4. The logarithmic variation of the determinate R_g and R_{gb} values for $La_{0.5}Sm_{0.2}Sr_{0.3}Mn_{0.85}Cr_{0.15}O_3$ with the inverse of temperature for the samples is shown in Fig. 9c. The Arrhenius law was applied in $\log(R_g; R_{gb})$ *vs.* $(1000/T)$ curves to estimate the activation energies (see Fig. 9c). The obtained (E_{Rgb}) values were closed to those deduced from dc conductivity and relaxation

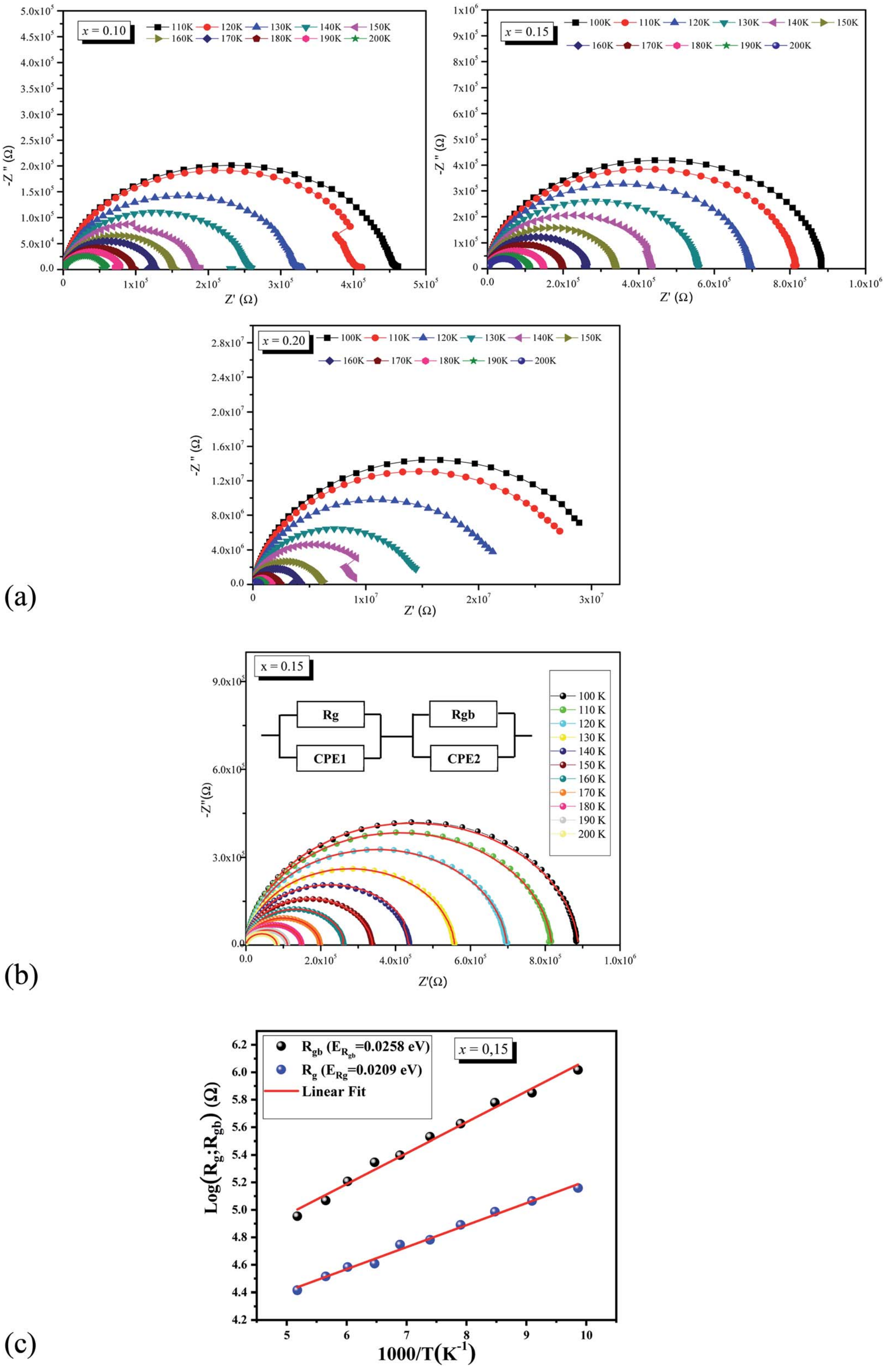

Fig. 9 a) Complex impedance plots for $La_{0.5}Sm_{0.2}Sr_{0.3}Mn_{1-x}Cr_xO_3$ ($x = 0.10$, 0.15 and 0.20) at various temperatures. (b) Complex impedance spectra for $La_{0.5}Sm_{0.2}Sr_{0.3}Mn0._{85}Cr_{0.15}O_3$ fitting using *Zview* software. *Inset*: the appropriate equivalent electrical circuit. (c) Variation of log(R_g; R_{gb}) *vs.* (1000/*T*) for $La_{0.5}Sm_{0.2}Sr_{0.3}Mn_{1-x}Cr_xO_3$ ($x = 0.15$).

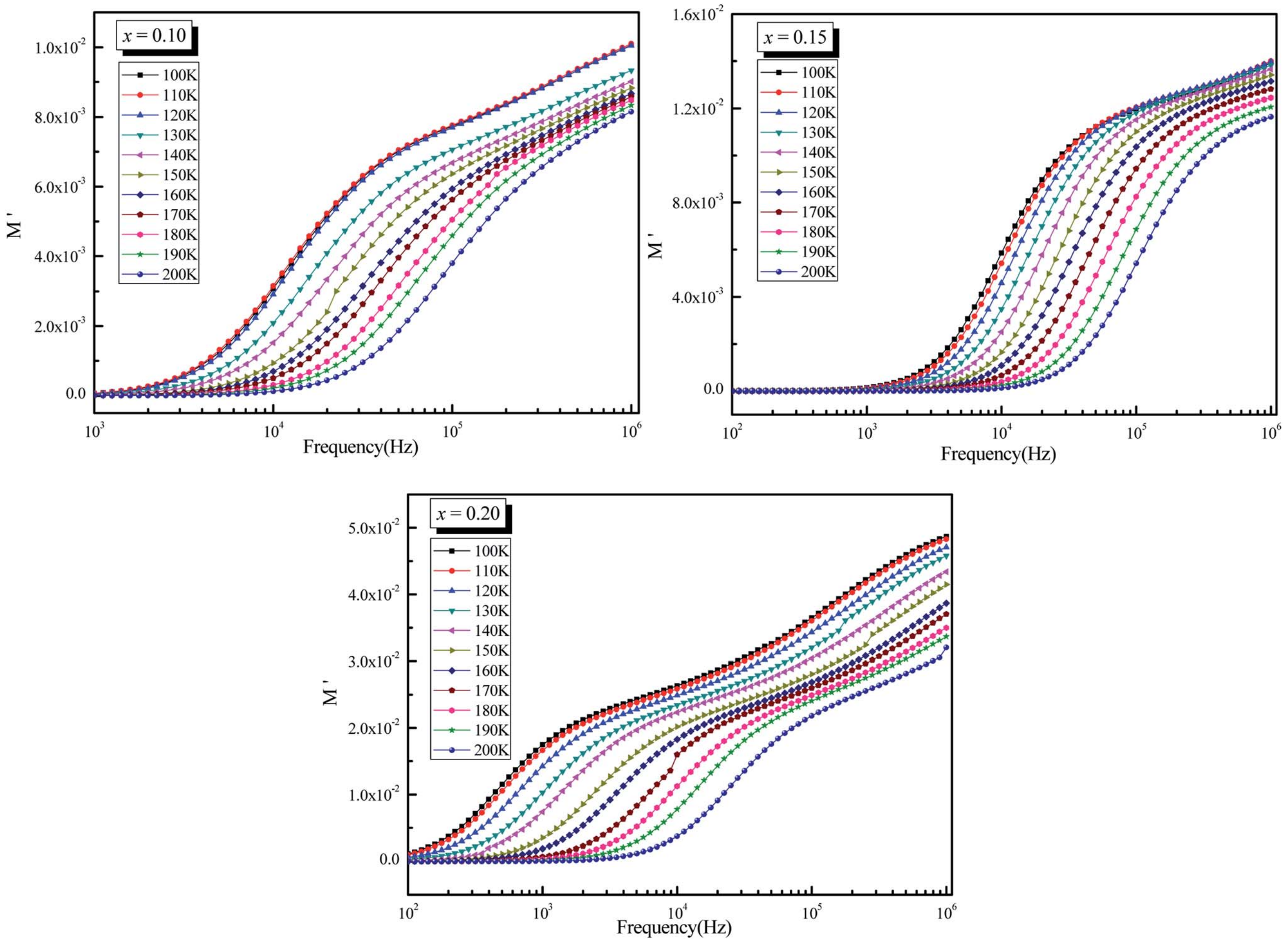

Fig. 10 Variation of real part of modulus (M') as a function of frequency (ω) at different temperatures for $La_{0.5}Sm_{0.2}Sr_{0.3}Mn_{1-x}Cr_xO_3$ ($x = 0.10$, 0.15 and 0.2).

time analyses. In addition, the grain boundary have a greater activation energy then grain which affirmed that grain boundary is less thermally conductive than its grain counterpart.

3.5 Complex modulus analysis

Fig. 10 shows the evolution of the real part of the electrical modulus with frequency at different temperatures for $La_{0.5}Sm_{0.2}Sr_{0.3}Mn_{(1-x)}Cr_xO_3$ (x = 0.10, 0.15 and 0.2). The M values for all samples are relatively low in the low frequency band, indicating that electrode polarization has a negligible effect on the materials.[69] With increasing frequency, M' displays a constant dispersion. This might be owing to charge carriers' short-range mobility.[70] For all of the temperatures in these figures, M' approaches a constant value (M) at high frequencies and it shows relaxation process, which occurs in the materials.

Fig. 11 depicts a semi-log plot of M'' *vs.* frequency for various compositions at various temperatures. The following describes the variation of M'' as a function of frequency:

- As the temperature rises, the maximum M'' max shifts to the higher frequency side, implying that dielectric relaxation is a thermally stimulated process. The modulus spectrum of various ionic conductors has been shown to have this effect.
- For the three compounds, two well defined broad and asymmetric peaks in M'' are found, suggesting the presence of

Table 4 Electrical parameters of equivalent circuit deduced from complex impedance spectra for different temperatures for $La_{0.5}Sm_{0.2}Sr_{0.3}Mn0._{85}$ $Cr_{0.15}O_3$

				CPE	
T (K)	R_g (10^5 Ω)	C (10^{-11} F)	R_{gb} (10^5 Ω)	Q (10^{-9F})	α_{bg}
100	1.2423	2.1977	7.7318	8.1964	0.67131
110	1.1613	2.1699	7.095	8.1975	0.67204
120	1.0369	2.1612	6.0102	7.4496	0.67941
130	4.7636	2.1796	0.86589	6.3352	0.691
140	0.60507	2.1917	3.7993	5.4903	0.70187
150	0.55863	2.2301	2.8487	5.0954	0.70812
160	0.40614	2.284	2.2207	3.5807	0.73132
170	0.38383	2.3675	1.6142	3.0695	0.74174
180	0.32781	2.4934	1.1694	2.0766	0.76509
200	0.22608	2.894	0.60606	0.8142	0.81783

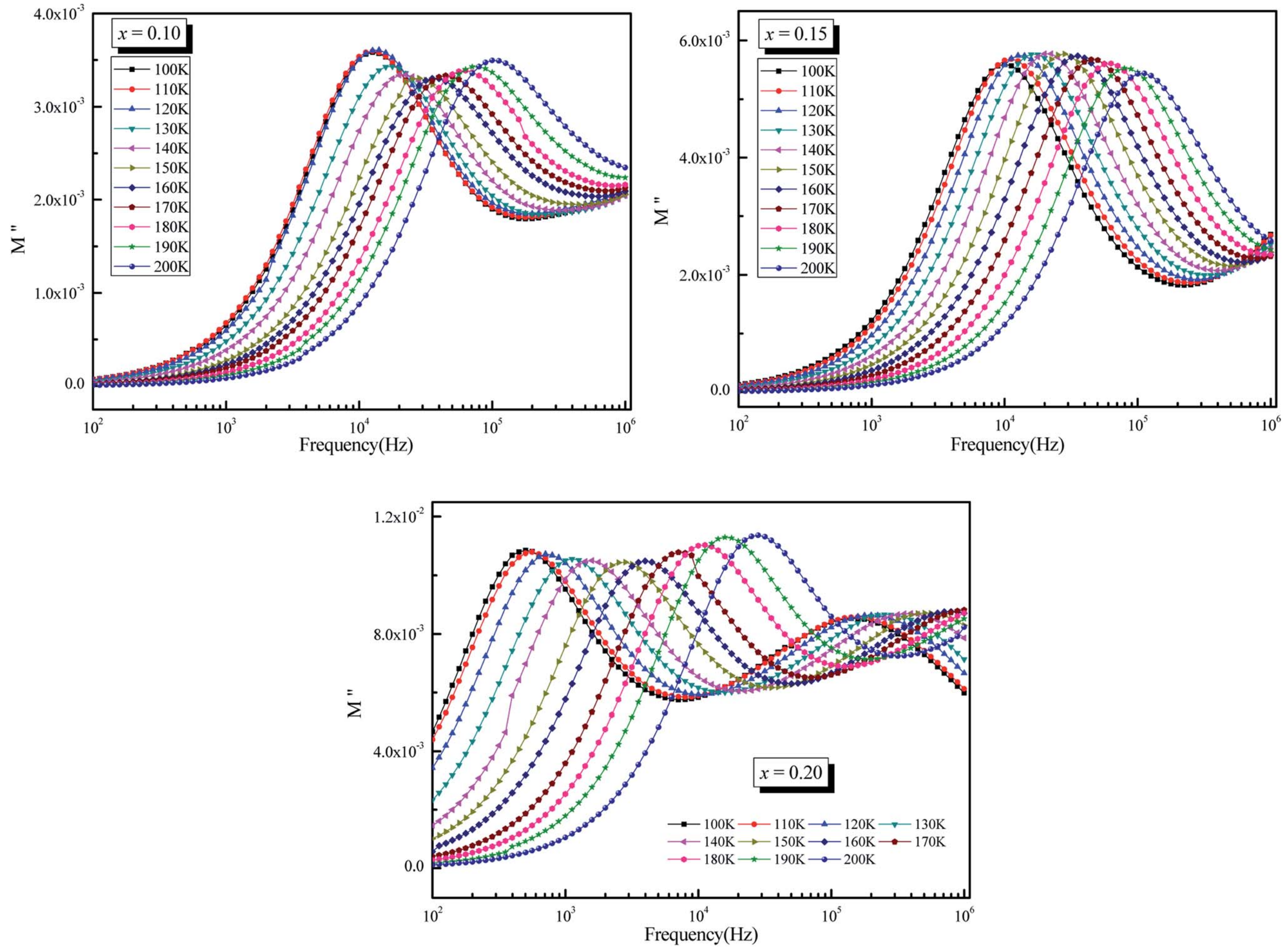

Fig. 11 Variation of imaginary part of modulus (M'') as a function of frequency (ω) at different temperatures for $La_{0.5}Sm_{0.2}Sr_{0.3}Mn_{1-x}Cr_xO_3$ (x = 0.10, 0.15 and 0.2).

two relaxation processes which illustrates the existence of non-Debye type relaxation. With rising temperature, these two relaxation peaks progressively overlapped at high frequency. $M''(f)$ curves for (x = 0.10 and 0.15) were modeled using the Kohlrausch, Williams and Watts (KWW) function[71] Fig. 12a:

$$M'' = \frac{M''_{1\max}}{\left((1-\beta_1)+\left(\frac{\beta_1}{1+\beta_1}\right)\right)\left[\left(\frac{f_{1\max}}{f}\right)+\left(\left(\frac{f}{f_{1\max}}\right)^{\beta_1}\right)\right]} + \frac{M''_{2\max}}{\left((1-\beta_2)+\left(\frac{\beta_2}{1+\beta_2}\right)\right)\left[\left(\frac{f_{2\max}}{f}\right)+\left(\left(\frac{f}{f_{2\max}}\right)^{\beta_2}\right)\right]} \tag{17}$$

where $M''_{\max}$ represent the peak maxima and $f_{\max}$ its corresponding frequency, β_1 and β_2 are the stretching factors which rank between 0 and 1.[71] The $M''(f)$ data were well fitted using eqn (17) as shown in Fig. 12a for both compounds (x = 0.10 and 0.15). The β_1 and β_2 values are less than unity which confirms the non-Debye dielectric behavior of the samples.

Fig. 12b depicts the variation of β_1 with temperature for the samples (x = 0.10 and 0.15), β_1 values increase when temperature rises. The decrease of β_1 values with Cr content can be related to the increase of grains size.[72] The relaxation time (τ) was calculated from the relaxation frequency ($f_{\max}$) through the following relation:

$$\tau = 1/2\pi f_{\max} \tag{18}$$

Fig. 12c shows the $\log(\tau_{M''})$ *vs.* $(1000/T)$ curves which have also been modelized using the following Arrhenius equation:[73]

$$\tau_{M''} = \tau_0 \exp\left(\frac{E_{M''}}{k_B T}\right) \tag{19}$$

with τ_0 is a pre-exponential factor. The linear fit of the curves using eqn (19) allowed us to estimate the values of the activation energy ($E_{M''}$) as 0.0239 eV for x = 0.10, 0.260 eV for x = 0.15 and 0.289 eV for x = 0.20. These values correspond well with the estimated ones from the *dc* conductivity study.

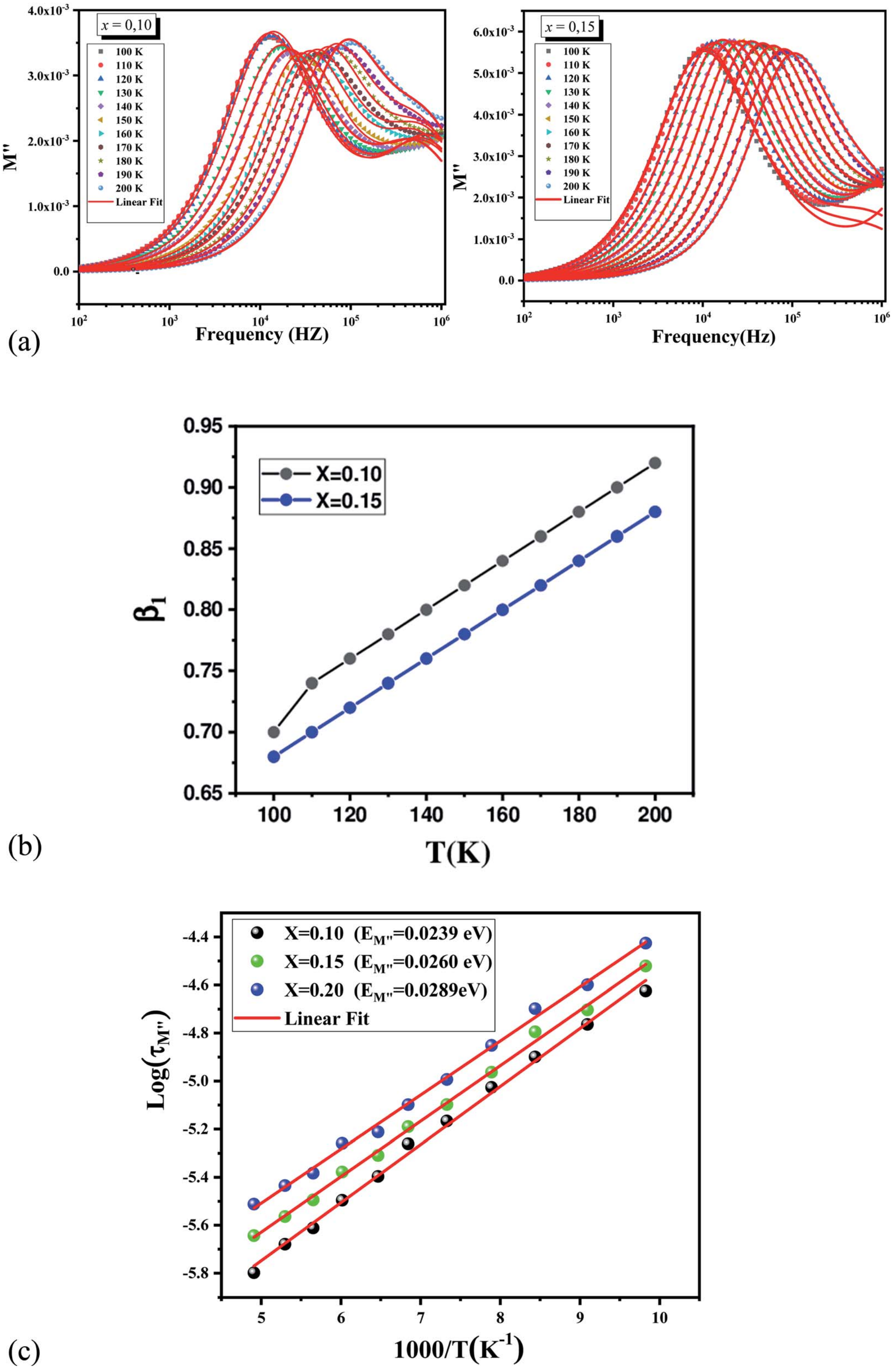

Fig. 12 (a) Frequency dependence at different temperatures of imaginary part (M'') of electrical modulus for $La_{0.5}Sm_{0.2}Sr_{0.3}Mn_{1-x}Cr_xO_3$ ($x = 0.10$ and 0.15). Red solid lines represent the fitting to the experimental data of $M''(f)$ using KWW function. (b) Variation of β_1 *vs.* temperature for $La_{0.5}Sm_{0.2}Sr_{0.3}Mn_{1-x}Cr_xO_3$ ($x = 0.10$ and 0.15). (c) Variation of $\log(\tau_{M''})$ *vs.* (1000/T). Red solid line is the linear fit for the data.

4. Conclusion

To sum up, polycrystalline $La_{0.5}Sm_{0.2}Sr_{0.3}Mn_{1-x}Cr_xO_3$ ($x = 0.10$, 0.15 and 0.20) manganites were synthesized using self-combustion process. The effects of the partial substitution of Mn^{3+} with Cr^{3+} on the structural, electrical and dielectrical properties of the investigated samples were carefully studied by means of X-ray diffraction analyses and complex impedance spectroscopy in the temperature range 100–400 K and in the frequency range of 100 Hz to 1 MHz. The X-ray diffraction analysis revealed that all samples exhibit single perovskite with orthorhombic *Pnma* structure. We have studied the electrical conductivity of our samples, it was found decreases with chrome content. It was verified that both dielectric losses ε'' and dielectric losses tangent tan δ decrease by increasing frequency and increase sharply at low frequency by increasing temperature. Nyquist plots confirmed the contributions of grain and grain boundary effect to the conductivity of the investigated samples.

Conflicts of interest

There are no conflicts to declare.

Acknowledgements

This research has been funded by the research Deanship of the University of Ha'il, project number RG-20 085.

References

1 A. Berksoy-Yavuz, E. Mensur-Alkoy, E. Erdem and S. Alkoy, *Ceram. Int.*, 2020, **48**, 28986.

2 H. SuHan, J. Koruza, E. A. Patterson, J. Schultheiß, E. Erdem, W. Jo, J.-S. Lee and J. Rödel, *J. Eur. Ceram. Soc.*, 2017, **37**, 2089.

3 A. Nucara, F. MilettoGranozio, W. S. Mohamed, A. Vecchione, R. Fittipaldi, P. P. Perna, M. Radovic, F. M. Vitucci and P. Calvani, *Physica B*, 2014, **433**, 106.

4 Y. Bitla, S. N. Kaul and L. FernándezBarquín, *Physica B*, 2014, **448**, 225.

5 H. Rahmouni, A. Dhahri and K. Khirouni, *J. Alloys Compd.*, 2014, **591**, 262.

6 K. Abdouli, W. Cherif, M. A. Valent, M. P. F. Graça, L. Ktari, O. Messaoudi, S. Elgharbi and W. I. Elsofany, *J. Mater. Sci.: Mater. Electron.*, 2021, **32**, 22106–22118.

7 Kh. Abdouli, W. Cherif, H. Omrani, M. Mansouri, M. A. Valent, M. P. F. Graça and L. Ktari, Structural, magnetic and magnetocaloric properties of La0.5Sm0.2Sr0.3Mn1-xFexO3 compounds with (0 ≤ x ≤ 0.15), *J. Magn. Magn. Mater.*, 2018, **475**, 635–642.

8 F. Khammassi, *et al*, *J. Phys. D: Appl. Phys.*, 2021, **54**, 175001.

9 Kh Abdouli, *et al.*, *J. Alloys Compd.*, 2018, **739**, 1048–1058.

10 F. Khammassi, W. Cherif, A. J. M. Sales, K. Riahi, M. P. F. Graça and M. Dammak, *J. Supercond. Novel Magn.*, 2021, **34**, 497–505.

11 S. Aydi, W. Chérif, F. Khammassi, A. J. M. Sales, N. M. Ferreira and N. Zouari, *Appl. Phys. A*, 2021, **127**, 931.

12 S. Khadhraoui, A. Triki, S. Hcini, S. Zemni and M. Oumezzine, Variable-range-hopping conduction and dielectric relaxation in Pr0.6Sr0.4Mn0.6Ti0.4O3±δ perovskite, *J. Magn. Magn. Mater.*, 2014, **371**, 69–76.

13 R. Selmi, W. Cherif, A. R. Sarabando, N. M. Ferreira and L. Ktari, *J. Mater. Sci.: Mater. Electron.*, 2022, **33**, 1703–1723.

14 R. Tlili, R. Hammouda, M. Bejar and E. Dhahri, Theoretical investigation of the magnetocaloric effect on La0.7(Ba, Sr) 0.3Mn0.9Ga0.1O3 compound at room temperature, *J. Magn. Magn. Mater.*, 2015, **386**, 81.

15 J. J. Blanco, M. Insausti, I. Gil de Muro, L. Lezama and T. Rojo, Neutron diffraction and magnetic study of the Nd0.7Pb0.3Mn1-xFexO3 (0≤x≤0.1) perovskites, *Solid State Chem.*, 2006, **179**, 623.

16 M. Bejar, R. Dhahri, E. Dhahri, M. Balli and E. K. Hlil, Large magnetic entropy change at room temperature in La0.7Ca0.3-xKxMnO3, *J. Alloy. Compd.*, 2007, **442**, 136.

17 L. Chick, L. Pederson, G. Maupin, J. Bates, L. Thomas and G. Exarhos, *Mater. Lett.*, 1990, **10**(1–2), 6.

18 R. Peng, X. Fan, Z. Jiang and C. Xia, *Fuel Cells*, 2006, **6**(6), 455.

19 C. C. Hwang and T. Y. Wu, *J. Mater. Sci. Eng. B*, 2004, **111**(2–3), 197.

20 S. Jain, K. Adiga and V. P. Verneker, *Combust. Flame*, 1981, **40**, 71.

21 R. D. Shannon, Revised effective ionic radii and systematic studies of interatomic distances in halides and chalcogenides, *Acta Crystallogr., Sect. A: Cryst. Phys., Diffr., Theor. Gen. Crystallogr.*, 1976, **32**(5), 751–767.

22 A. Taylor, *X-Ray Metallography*, Wiley, New York, 1961.

23 J. S. Rathod, M. J. Keshvani, P. S. Solanki, D. D. Pandya, B. Kataria, N. A. Shah and D. G. Kuberkar, *Phys. B*, 2015, **478**, 1.

24 A. K. Jonscher, *Nature*, 1977, **267**, 673.

25 X. F. Du and I. W. Chen, *J. Am. Ceram. Soc.*, 1998, **81**, 3253.

26 J. Zhang, Q. Yan, F. Wang, P. Yuan and P. Z. Hang, *J. Phys.: Condens. Matter*, 2000, **12**, 1981.

27 P. V. Vanitha, R. S. Sing, S. Natarajan and C. N. R. Rao, *J. Solid State Chem.*, 1998, **137**, 365.

28 A. Maignan, C. Martin, F. Damay, M. Hervieu and B. Raveau, *J. Magn. Magn. Mater*, 1998, **188**, 185.

29 K. Funke, *Prog. Solid State Chem.*, 1993, **22**, 111–195.

30 A. Selmi, S. Hcini, H. Rahmouni, A. Omri, M. L. Bouazizi and A. Dhahri, *Phase Transitions*, 2017, **90**, 942.

31 M. H. Dhaou, S. Hcini, A. Mallah, M. L. Bouazizi and A. Jemni, *Appl. Phys. A: Mater. Sci. Process.*, 2017, **123**, 8.

32 F. Hcini, S. Hcini, B. Alzahrani, S. Zemni and M. L. Bouazizi, *J. Mater. Sci.: Mater. Electron.*, 2020, **31**, 14986–14997.

33 W. K. Lee, J. F. Liu and A. S. Nowick, *Phys. Rev. Lett.*, 1994, **67**, 1559.

34 S. R. Elliott, *Adv. Phys.*, 1987, **36**, 135; S. R. Elliott, *Solid State Ionics*, 1994, **27**, 70–71.

35 A. Dhahri, A. Zaouali, A. Benali, N. Abdelmoulla, J. Massoudi, K. Nouri, L. Bessais, M. P. F. Graça, M. A. Valente and B. F. O. Costa, *J. Mater. Sci.: Mater. Electron.*, 2021, **32**, 7926–7942.

36 S. Khadhraoui, A. Triki, S. Hcini, S. Zemni and M. Oumezzine, *J. Magn. Magn. Mater.*, 2014, **371**, 69–76.

37 M. Pollak, *Philos. Magn.*, 1971, **23**, 519.

38 S. Mollah, K. K. Som, K. Bose and B. K. Chaudhuri, *J. Appl. Phys.*, 1993, **74**, 931.

39 A. Ghosh, *Phys. Rev. B: Condens. Matter Mater. Phys.*, 1990, **41**, 1479.

40 M. Megdiche, C. Perrin-Pellegrino and M. Gargouri, *J. Alloys Compd.*, 2014, **584**, 209.

41 A. Banerjee, S. Pal and B. K. Chaudhuri, *J. Chem. Phys.*, 2001, **115**, 1550.

42 A. Banerjee, S. Pal, S. Bhattacharya, B. K. Chaudhuri and H. D. Yang, *Phys. Rev. B: Condens. Matter Mater. Phys.*, 2001, **64**, 104428.

43 F. B. Abdallah, A. Benali, S. Azizi, M. Triki, E. Dhahri, M. P. F. Graça and M. A. Valente, *J. Mater. Sci. Mater. Electron.*, 2019, **30**, 8457.

44 M. H. Dhaou, S. Hcini, A. Mallah, M. L. Bouazizi and A. Jemni, *Appl. Phys. A*, 2017, **123**, 8.

45 A. Benali, M. Bejar, E. Dhahri, M. F. P. Graça and L. C. Costa, *J. Alloys Compd.*, 2015, **653**, 506.

46 A. K. Roy, A. Singh, K. Kumari, K. Amar Nath, A. Prasad and K. Prasad, *ISRN Ceram*, 2012, **2012**, 1–10.

47 N. F. Mofft and E. A. Davis, *Electronic Processes in Non-Crystalline Materials*, Oxford, Great Britain, 1979.

48 J. C. Maxwell, *Electricity and Magnetism*, Oxford University Press, London, 1973.

49 K. W. Wagner, *Ann. Phys.*, 1913, **40**, 817.

50 J. H. Joshi, G. M. Joshi, M. J. Joshi and K. D. Parikh, *Ionics*, 2019, **25**, 3245.

51 P. A. Jadhav, R. S. Devan, Y. D. Kolekar and B. K. Chougule, *J. Phys. Chem. Solids*, 2009, **70**, 396.

52 J. C. Giuntini, J. V. Zanchetta, D. Jullien, R. Eholie and P. Houenou, *J. Non-Cryst. Solids*, 1981, **45**, 57.

53 J. R. Macdonald, *Impedance Spectroscopy Emphasizing Solid Materials and Systems*, 1987.

54 J. H. Joshi, D. K. Kanchan, M. J. Joshi, H. O. Jethva and K. D. Parikh, *Mater. Res. Bull.*, 2017, **93**, 73.

55 H. Ye and R. B. Jackman, *J. Appl. Phys.*, 2003, **94**, 7878.

56 P. B. Macedo, C. T. Moynihan and R. Bose, *Phys. Chem.*, 1972, **13**, 171.

57 J. H. Joshi, G. M. Joshi, M. J. Joshi, H. O. Jethvaa and K. D. Parikh, *New J. Chem.*, 2018, **42**, 17249.

58 V. Provenzano, L. P. Boesch, V. Volterra, C. T. Moynihan and P. B. Macedo, *J. Am. Ceram. Soc.*, 1972, **55**, 492.

59 H. Jain and C. H. Hsieh, *J. Non-Cryst. Solids*, 1994, **172**, 1408.

60 A. K. Jonscher, The 'universal' dielectric response, *Nature*, 1977, **267**, 673–679.

61 M. A. Valente, M. Peres, C. Nico, T. Monteiro, M. P. F. Graça, A. S. B. Sombra and C. C. Silva, *Opti. Mat.*, 2011, **33**, 1964.

62 D. C. Sinclair and A. R. West, *J. Appl. Phys.*, 1989, **66**, 3850.

63 M. A. L. Nobre and S. Lanfredi, *J. Appl. Phys.*, 2003, **93**, 5557.

64 S. K. Rout, S. Parida, E. Sinha, P. K. Barhai and I. W. Kim, *Curr. Appl. Phys.*, 2010, **10**, 917.

65 K. S. Cole and R. H. Cole, *J. Chem. Phys.*, 1941, **9**, 341.

66 J. R. Macdonald, *Impedance Spectroscopy Emphasizing Solid Materials and Systems*, 1987.

67 J. H. Joshi, D. K. Kanchan, H. O. Jethva, M. J. Joshi and K. D. Parikh, *Ionics*, 2018, **24**, 2016.

68 B. Behera, P. Nayak and R. N. P. Choudhary, *Mater. Res. Bull.*, 2008, **43**, 401–410.

69 N. H. Vasoya, P. K. Jha, K. G. Saija, S. N. Dolia, K. B. Zankat and K. B. Modi, *J. Electron. Mater.*, 2016, **45**, 917.

70 B. Behera, P. Nayaka and R. N. P. Choudhary, *Mater. Chem. Phys.*, 2007, 106–193.

71 C. B. Mohamed, K. Karoui, S. Saidi, K. Guidara and A. B. Rhaiem, *Physica B*, 2014, **451**, 87.

72 N. Sivakumar, A. Narayanasamy, N. Ponpandian and G. Govindaraj, *J. Appl. Phys.*, 2007, **101**, 084116.

73 S. Hcini, A. Omri, M. Boudard, M. L. Bouazizi, A. Dhahri and K. Touileb, *J. Mater. Sci.: Mater. Electron.*, 2018, **29**, 6879.